Int. J. Electrochem. Sci., 14 **(2019)** 5613 – 5628, doi: 10.20964/2019.06.27

International Journal of
ELECTROCHEMICAL
SCIENCE
www.electrochemsci.org

Phosphomolybdic Acid coupling with Vulcan XC72 Carbon as Superior Catalyst to Enhance ORR Activity and Performance of MFC

Kai Zhang[2], *Yongkui Huang*[2], *Daijun Zhang*[1,2,*], *Aqiang Ding*[1,2], *Xiaoting Zhang*[2], *Peili Lu*[1,2]

[1] Key Laboratory of Coal Mine Disaster Dynamics and Control, Chongqing University, Chongqing, 400044, PR China.
[2] College of Resource and Environmental Science, Chongqing University, Chongqing, 40044, PR China.
[*]E-mail: dzhang@cqu.edu.cn

Received: 6 February 2019 / *Accepted:* 31 March 2019 / *Published:* 10 May 2019

Microbial fuel cell (MFC) is an emerging technology that can treat wastewater and recover energy simultaneously However, there are many factors that limit its application, among which cathode catalysts are one of the main obstacles. In this study, $H_3PMo_{12}O_{40}$/Vulcan XC72 carbon (PMo/CB) material was successfully prepared by a feasible process and used as efficient catalyst on oxygen reduction reaction (ORR) to improve the performance of MFC. The electrochemical performance of PMo/CB and Pt/C were evaluated by LSV, EIS, and Tafel plot. The results showed that the ORR activities of samples were following the order of PMo/CB-2 > Pt/C > PMo/CB-3 > PMo/CB-1 > PMo/CB-4 > CB. Moreover, PMo/CB exhibited a high durability compared to Pt/C in MFC after 4 months of operation. Finally, the catalytic reaction mechanism of PMo/CB was discussed. The results demonstrated the high ORR activity of the sample could be attributed to the favorable specific surface area of CB and the effect of electrostatic coupling between PMo and CB, which enhanced the adsorption and reduction of O_2. Therefore, PMo/CB will be a promising cathode ORR catalyst for microbial electrochemical system.

Keywords: Phosphomolybdic acid, Vulcan XC72 carbon, Oxygen reduction reaction, Microbial fuel cells.

1. INTRODUCTION

Microbial fuel cell (MFC) has been intensively studied as a sustainable bio-electrochemical technology for wastewater treatment and energy recovery [1, 2], in which the electroactive electrogenic bacteria attached to the surface of the anode to generate electricity [3]. However, cathodic reaction is the major limiting factor for MFC performance [4]. In recent years, much more research has been engaged to overcome the limitations of the cathodic reaction. Among them, air-cathodes have attached great

attention due to its advantages of high productivity, lower internal resistance, non-toxic products (H_2O) and sustainability [5]. However, the catalyst of air-cathode is one of the main factors that limits its performance. Until now, platinum-based catalysts are the most efficient catalyst, which can reduce the overpotential generated by the ORR and improve the catalytic efficiency [6, 7]. However, they are very expensive, contain precious metal and declining activity. These problems have severely hindered the commercialization of large-scale MFCs [8, 9]. Therefore, the development of high-performance and low-cost ORR catalyst has become an urgent problem to be solved.

In the past few decades, carbon-base materials have been widely used as catalysts due to their low cost and good stability [10-12]. However, the carbon materials cannot be directly used as a catalyst owing to its poor catalytic activity. Therefore, many modification methods have been investigated to improve their catalytic activity. Doping carbon is a method for improving the catalytic activity of carbon-based materials. It has been reported that nitrogen-, phosphorus- and sulfur-doped carbon have a high efficient activity and stability for ORR [13-16]. However, their catalytic activities are still unsatisfactory for the practical application of MFC. Using carbon as support is also a strategy to improve its catalytic activity, such as Co-Ppy/C [17], Pd/C [18], transition metal/carbon nanoparticle [19]. Their catalytic activities and stability can be effectively controlled by regulating the amount of active substance [20]. Therefore, carbon materials are the promising supports for designing novel material with high catalytic activity.

Polyoxometalates (POMs) constituted a large class of nanoscale transition metal (d blocks) - oxygen clusters [21-27], have been applied in various catalysts due to their multiple properties, such as a stable microstructure, effective electronic pathway, good proton conductivity, inexpensive and pollution-free [28, 29]. Phosphomolybdic acid ($H_3PMo_{12}O_{40}$, PMo) is a kind of POM with the typical Keggin structure, and has been used as a multivariate material [30]. Nevertheless, the lower specific surface area and high solubility of POM in electrolytes remain the most critical challenge in its practical application [31]. POM can be immobilized on carbon material or metal oxide to obtain catalysts with high catalytic activity and stability. Xin et al [32] prepared POM/Au-nanoparticle hybrid as a catalyst for ORR, which could achieve higher catalytic activity and stability. Diana M et al [33] combined $Co_4(PW_9)_2$ with carbon nanomaterials to obtain lower Tafel slope and 2-electron and 4-electron mixing mechanism in the ORR process. Vulcan XC72 is one of the most widespread in carbon materials for catalyst, because of cost-effective and good availability [34]. However, few reports have been found to couple PMo with Vulcan XC72 as catalyst for ORR. Considering the stable Keggin structure and excellent electron transfer capability of PMo, it is anticipated that the incorporation of PMo with Vulcan XC-72 will be employed in catalyst by taking the advantages of large specific surface and high electron conduction of Vulcan XC-72. Besides, to the best of our knowledge, PMo/CB has been rarely applied in MFC.

In this work, the $H_3PMo_{12}O_{40}$/CB (PMo/CB) was synthesized by internal electrostatic interaction as air-cathode ORR catalyst of MFC. The surface structures and chemical composition of PMo/CB were characterized by X-ray diffraction (XRD), X-ray photoelectron spectroscopy (XPS), FT-IR and Brunauere-Emmette-Teller (BET). The electrochemical performance of as-prepared catalyst was investigated by linear sweep voltammetry (LSV), electrochemical impedance spectroscopy (EIS) and Tafel plots in an electrolyte of 50 mM phosphate buffer solution (PBS, pH=7). Furthermore, PMo/CB

was used as the catalyst of air-cathode in MFCs to study the catalytic performance. The results have shown that PMo/CB-2 achieved higher catalyst performance for ORR and significantly improved durability in comparison to the commercial Pt/C (10 wt%) in MFC. Finally, the catalytic mechanism of PMo/CB was also discussed. PMo/CB exhibited excellent catalytic activity for the ORR due to strong surface interaction between PMo and carbon atoms. The obtained results demonstrated PMo/CB can be a promising air-cathode catalyst for microbial electrochemical system.

2. MATERIALS AND METHODS

2.1. Synthesis of PMo/CB

Putting 144.00 g of MoO_3 and 9.57 g of 85% H_3PO_4 into1400 mL of deionized water, stirred and refluxed for 30 minutes. After the boiling shrimp was stirred for 3 hours, a few drops of bromine water was added to the solution and filtered out the mother liquor. The liquor was concentrated to obtain crystal for 3-4 hours. After that, the crystal was dried under vacuum to obtain crude product. Then, the crude product was dissolved in 100 mL of deionized water and filtered to obtain clear liquid, which was allowed to stand for volatilization to be crystallized, and dried at room temperature to obtain phosphomolybdic acid ($H_3PMo_{12}O_{40}$).

Vulcan XC-72 carbon (CB) was completely immersed in 80 mL of 1 mol/L nitric acid for 24 h at room temperature (25°C). The treated CB was washed with deionized water for several times and supernatant was removed by centrifugation at 4500 rpm for 15 min. Then put it into an oven at 120°C for 12 h. Hereafter, adding 0.053, 0.11, 0.25, 0.50 and 1.00 g of synthetic PMo into the 1.00 g treated CB which dispersed in ethanol for 15 minutes after ultrasonication respectively, and stirred for 24 hours on a magnetic stirrer after 30 minutes of ultrasonication. Baking in an oven at 120 °C for 5-6 h. A series of PMo/CB (5.0 wt%, 10.0 wt%, 33.3 wt%, and 50.0 wt%) were obtained and were labeled PMo/CB-1, PMo/CB-2, PMo/CB-3 and PMo/CB-4, respectively.

2.2. Characterizations

Powder X-ray diffraction (XRD) analysis was carried out a XRD instrument (XRD-6000. Japan) using Cu Kα radiation (λ= 0.15418nm). X-ray photoelectron spectroscopy (XPS) analysis was recorded on a XSAM 800-spectrometer using a standard Al K X-ray source (1486 eV). FT-IR spectroscopy was conducted by FT-IR spectrometer (Thermo Fisher MultiGas 6030). Brunauer Emmett Teller (BET) of the PMo/CB was tested by using a Micromeritics (ASAP 2020M, USA) instrument.

2.3. Electrochemical measurements

All electrochemical data were obtained on an electrochemical workstation (CHI1660E, Shanghai Chenhua Co., Ltd) with a routine three-electrode system. The carbon cloth electrode, a platinum wire (99.99%, 5cm) and an Ag/AgCl electrode (3 M KCl, +0.21 V vs a standard hydrogen electrode) were

used as working electrode, counter electrode and reference electrode, respectively. 50 mM PBS [6] (4.57 g/L Na_2HPO_4, 0.31 g/L NH_4Cl, 0.13 g/L KCl, 2.7695 g/L $NaH_2PO_4 \cdot 2H_2O$) was used as the electrolyte. Linear sweeping voltammetry (LSV) was measured at 5 mV/s between 0.1 to -0.8 V. Electrochemical impedance spectroscopy (EIS) were tested at -0.1 V over a frequency range set to 10000 HZ-0.001 HZ. Tafel plots were prepared to investigate the ORR kinetics of the sample, which were recorded by sweeping the overpotential from -0.1 V to 0.1 V at 1 mV/s. The rotating disk electrode (RDE) measurement was run at 5 mV/s between 0.3 to −0.8 V (vs Ag/AgCl) in an O_2-saturated 50 mM PBS solution by stepwise variation of rotating speed from 400-2500 rpm. Sample ink was prepared by adding 4.0 mg of powder into 0.8 mL of isopropanol, 0.2 mL of nafion (5 wt%), followed by sonicating for 30 min, and the suspension (14 μL) was applied to the rotating disc electrode (RDE, Φ= 5 mm), the sample loading was 0.28 mg cm^{-2}. The above operations were performed at room temperature (25°C).

2.4. Electrode preparation

All the carbon cloth cathodes were fabricated by the method of rolling-press. The diffusion layer was made of carbon black (Guangzhou Zhenwei Chemical Technology Co., Ltd. China) and PTFE (20 wt %) with a mass ratio of 1:6, followed by heating at 370 °C for 15 min and repeated the operation 4 times. Different PMo/CB powder were rolled and pressed on the back of carbon cloth diffusion layer with nafion (5 wt% solution) as binder (Hesen, Shanghai, China). Each PMo/CB was coated with three cathodes and air-dried for 24 hours at room temperature (25°C). The amount of PMo/CB were 25 mg/cm^2. In addition, Pt/C cathode (10% Pt, Hesen, Shanghai, China) was also made with the same method and Pt/C (10 wt%) loading was 5 mg/cm^2.

2.5. MFC Experiments

Cubic-shape single-chamber MFCs were constructed by plexiglass with the size of 10cm×5cm×5cm. Reactor inlet volume was 250 mL. The obtained PMo/CB electrode and carbon fiber were used as MFC's cathode and anode, respectively. All anodes were soaked in acetone solution for 12 h and then treated with 1000 mL of acid solution (100 mL H_2SO_4 and 200 g of $(NH_4)_2S_2O_8$) for 15min. Finally, the carbon fiber was calcinated for 30 minutes at 450 °C in the muffle furnace [35]. All MFC tests were performed in two copies. Anode-inoculated laboratory biofuel cell anolyte cultures with high salt (11 g/L) for more than 1 year. The composition of the medium contains 600 mg/L COD (CH_3COONa), 11000 mg/L NaCl, 100 mg/L KCl, 2500 mg/L $NaHCO_3$, vitamin solution: 10 mL/L, trace elements: 10 mL/L, the initial pH was 7. All MFCs were operated through batch experiments with a 1000 Ω external resistor in room temperature (25 °C).

The voltage (U) was recorded by using an external resistance box as an electrical appliance through a computerized data acquisition system (DAQ2213ADLINK, China). Polarization curves were obtained by altering different external resistance values, each applied resistance value was maintained for 30 minutes to ensure a stable potential. It was conducted after the MFCs had been operated for 1 month, by varying the external resistances (R) from 9000 to 20 Ω. Current densities (J) and power

densities (P) were calculated by two formulae: J = U/RA (Cathode projection area A=12.56 cm^2) and P =JU. Anode potentials tested by using an Ag/AgCl as reference electrode (+0.21 V vs a standard hydrogen electrode) [36].

3. RESULTS AND DISCUSSION

3.1. Structural characterization of the catalyst

The structures of the sample were verified by X-ray diffraction (XRD) experiments. Fig 1 showed that the XRD pattern of PMo exhibited seven peaks at 7.9° (1 1 0), 8.9° (0 -1 1), 17.7° (1 2 1), 18.5° (-2 0 2), 26.2° (1 -4 1), 27.8° (3 -1 1), 28.8° (-3 1 2) [37], and the corresponding chemical formula was $H_3PMo_{12}O_{40}$, which was the basic molecular formula of PMo. After PMo was coupled to CB, it emerged the diffractive characteristics of CB [38], and the main peak of PMo had an obvious weakening. Therefore, the results indicated PMo was successfully attached to the CB.

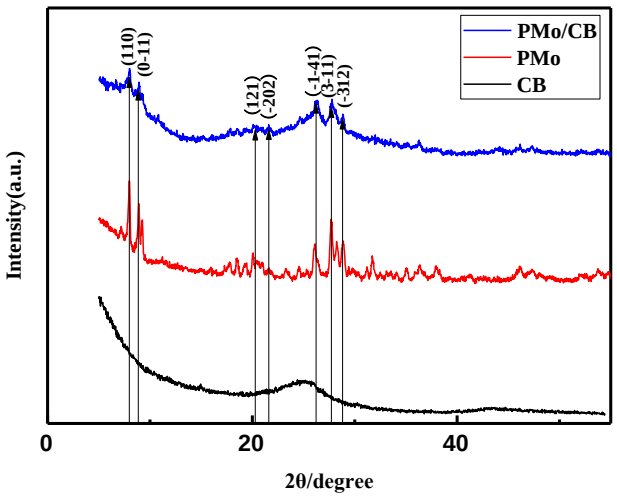

Figure 1. The XRD patterns of PMo/CB, PMo and CB

XPS was used to test the chemical composition of PMo/CB. Fig 2(a)-(d) showed the XPS results of the sample. The element composition of PMo/CB catalyst was identified from the full survey spectra (Fig 2(a)). Elemental signal of Mo, P, C and O could be found in the survey spectrum, and the results of relevant elemental content was calculated and listed in Table 1. Dramatically, the mole ratio of Mo/(P+Mo) and P/(P+Mo) were 98.29 and 1.71 respectively, which was nearly consistent with the stoichiometric coefficients of PMo (97.37 and 2.63), revealing PMo was successfully adsorbed on the CB. The inset of fig 2(b) showed Mo 3d spectral range can be divided into two valence states (Mo^{4+} and Mo^{6+}), with spectral positions at 232.2 eV and 235.5 eV. Mo^{6+} 3d3/2 mainly contains MoO_3 and Mo^{4+} came from MoO_2 and 4H-Mo (233.3 eV) [39]. The coexistence of transition metal in such different valence states significantly improved rate of electron conversion during ORR, thereby enhancing the ORR activity [40]. The peaks centered at high resolution C1s spectrum (Fig 2(c)) showed the presence of C-C (284.5 eV and 285.5 eV) and C-O (286.6 eV). The O1s spectrum (Fig 2(d)) can be deconvoluted

into three main peaks centered at 530.3, 531.4, and 532.7eV, assigned to Mo-O, C=O and C-O respectively. And there are little carbon-oxygen single bonds and carbon-oxygen double bonds on the surface of CB [41], which is suggested that carbon-oxygen bonds and carbon-oxygen double bonds structure have been created after the recombination. These results further confirmed that PMo was successfully loaded on the surface of the CB.

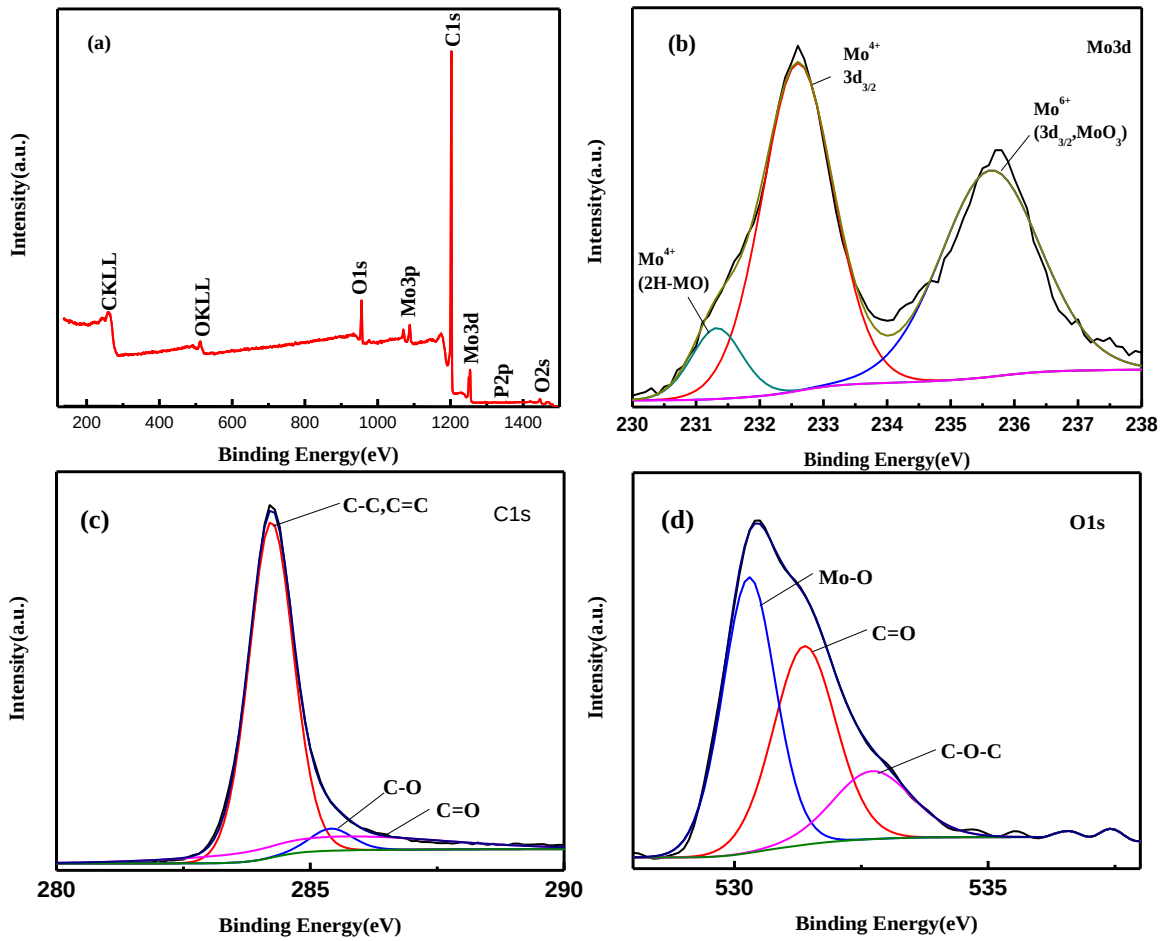

Figure 2. The XPS spectra of (a) PMo/CB and individual XPS spectrum of (b)Mo3d, (c)C1s and (d) O1s.

Table 1. The elemental analysis of PMo/CB based on the results of XPS.

Mo content (atomic, %)	P content (atomic, %)	Mo/(P + Mo)	n(Mo)/n(P + Mo)
98.29	1.71	98.29	97.37

The IR spectra of PMo, CB and PMo/CB were displayed in Fig 3. The spectra showed a broad band around 1750-2250 cm^{-1} for all of samples, which can be ascribed to the asymmetric stretching of the OH group [42]. The absorption band at 1500 -2500 cm^{-1} was due to the H-O-H bending vibration. The FT-IR spectra of PMo/CB showed bands of 1048, 949, 860 and 678 cm^{-1} were assigned to the

characteristic bands of Keggin structure, symmetric PO_4 tetrahedral stretching, asymmetric peripheral metal-atoms-terminal oxygen (Mo-O) and Mo-O-Mo. These bands were internally stretched and triple-metal bridged into an octahedral bridge [43,44]. This result demonstrated the typical structural characteristics of PMo were coated onto the surface of CB.

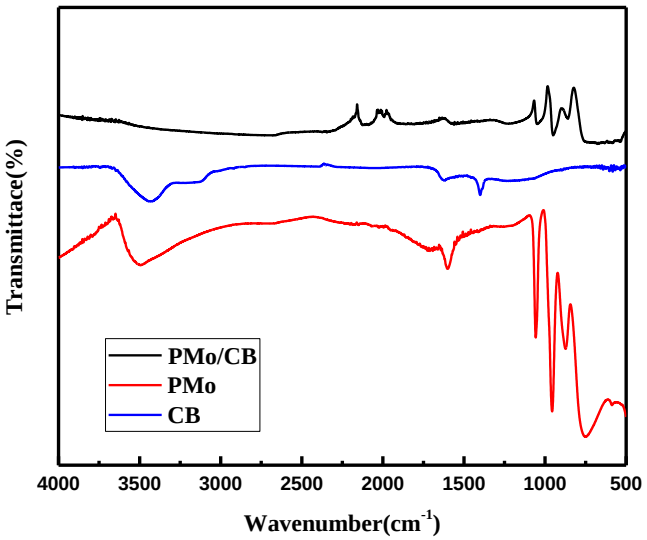

Figure 3. The FT-IR spectra of the PMo/CB, PMo and CB.

The high BET specific surface area of the catalyst was beneficial to contribute more oxygen molecule attachment points and active sites for ORR [45]. The specific surface area of PMo/CB were listed in table 2. It can be seen that the specific surface area of pure PMo was only 12.7m^2/g. When PMo was coupled to CB, the specific surface area sharply increased. These suggested that the CB provided more accessible active sites of PMo/CB by improving the specific surface area [46]. Moreover, these specific surface areas were even larger than some MOF-derived catalysts [47]. However, as the number of PMo in the sample increases further, its specific surface area decreases. It is also suggested that an increase of PMo on CB will reduce the specific surface area of the sample, and thus have a negative effect on the adsorption and reduction of oxygen for the sample.

Table 2. The specific surface area of samples

Samples	PMo	PMo/CB-1	PMo/CB-2	PMo/CB-3	PMo/CB-4
The specific surface area(m^2/g)	12.7	175.95	186.11	82.92	43.22

3.2. Electrochemical Performance of PMo/CB

The LSV curves of samples with different amount of PMo were showed in Fig 4(a). The onset potentials divert toward the positive direction. The limiting current densities increase when the amount of PMo from PMo/CB-1 to PMo/CB-2 increased, which gradually approaches and exceeds that of Pt/C. However, the ORR activity of the PMo/CB is continuously lowered with the increase mass of PMo in the sample. The decline of their ORR activities may be attributed to the reduction of internal specific surface area of the sample.

In order to accurately describe the mass-catalysts of catalytic activity for ORR, the current-mass density of PMo/CB were further compared by selecting -0.1 V, -0.2 V, and -0.4 V (versus Ag/AgCl). The result was shown in Fig 4(b). PMo/CB-2 exhibited the highest mass current density (0.85 mA mg^{-1}), which was 8 times and 1.14 times higher than that of CB and Pt/C at a potential of -0.4 V, suggesting that is more likely to adsorb and activate O_2 on its surface. The results exhibited a lower current-mass density under 5 wt% PMo loading conditions, indicating less PMo composition on the CB surface. According to the mass-current density relationship, the ORR activity of the sample was obtained as PMo/CB-2 > Pt/C > PMo/CB-3 > PMo/CB-1 > PMo/CB-4 > CB. These results revealed that the PMo had a great influence on the ORR activity of the sample.

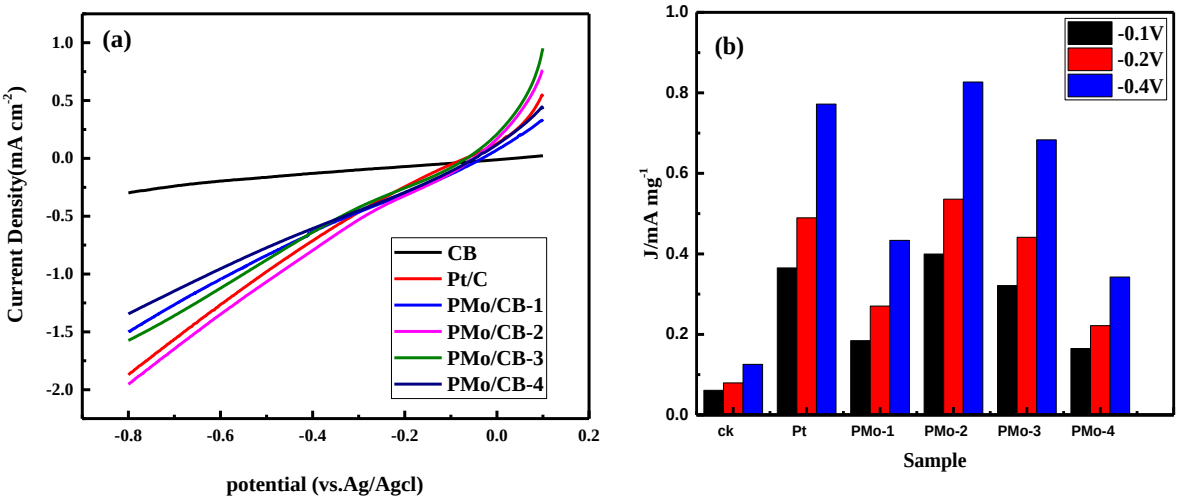

Figure 4. (a) LSV of PMo/CB at a scan rate of 5 mV/s in O_2-saturated 50mM PBS electrolyte. (b) current-mass density of PMo/CB at -0.1, -0.2, -0.4 V.

To gain deep insight into the electronic transfer mechanism of PMo/C-2 during the ORR process, the Koutecky-Levich (K-L) plots is derived from RDE data to calculate ORR electron transfers number (n) from the slope of fitting line, accroding to K-L Eq [48].

$$1/j = (nAFkC_0)^{-1} + (0.62nAFD_0^{2/3}v^{-1/6}C_0w^{1/2})^{-1}$$

RDE data of PMo/CB-2 at different rotation rate and were showed in fig 5(a). As the rotational speed increases, the limiting current densities increased due to the improved diffusion of O_2 on the electrode surface [49]. The K-L plots at -0.6--0.75V were illustrated with Figure 5(b). Based on the K-L equation, the number of electron transfer could be calculated. the n_{O2} values were almost constant in

the range of potentials between -0.6 and -0.75 versus Ag/AgCl, with estimated n_{O2} values of 3.69-3.9 for PMo/CB-2. These values were nearly identical to the n_{O2}=4.0 electrons toward the ORR estimated for the Pt/C (20 wt%). This suggested that the PMo/CB-2 conformed to a direct four-electron pathway during the ORR process. Therefore, these results further illustrated PMo coupling with CB played an important role in the catalytic process.

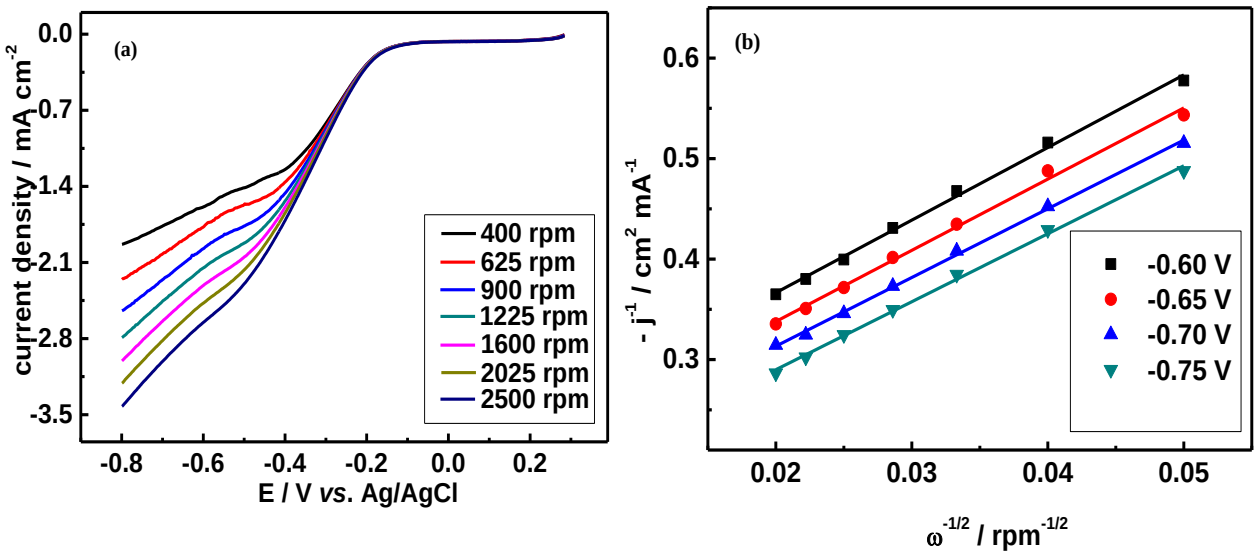

Figure 5. (a)LSV curve at different rotating speeds for PMo/CB-2 and (b) corresponding K-L plots at different potentials for RDE curves in O_2-saturated 50mM PBS.

To fully investigate the basic principles involved in promoting electrocatalytic activity toward ORR achieved by PMo/CB. The EIS and Tafel curve of samples were determined in this study. The nyquist plots (fig 6(a)) of different samples were analyzed and fitted by an equivalent circuit of the ohm resistance R_{ohm} (including the resistance of ions in the electrolyte, the intrinsic resistance of active materials and the contact resistance) and charge transfer resistance R_{act} [50-52]. The resistance values (ohm resistance and charge transfer resistance) were calculated by the equivalent circuit fitting and listed in the table 3. It can be seen that the coupling of PMo and CB reduced the impedance between the electrode and the electrolyte. The R_{act} of PMo/CB-2 was 21.4Ω, which was 2.2 times lower than that of CB. Besides, the PMo/CB-2 also achieved a lower R_{ohm} of 33.2Ω, which was 11.9 times lower than that of CB. Therefore, these results indicated that PMo coupling with CB possessed lower impedance and faster electron transfer capability, thus enhanced oxygen adsorption and diffusion during the ORR.

Generally, a higher exchange current density (i_0) means efficient catalytic rate for ORR and electron utilization. The Tafel curve was used to evaluate the electron transfer coefficient between the electrode and electrolyte. As shown in the figure 6(b), the Tafel lines became convergent and linear after a rapidly increased. Regression fitting of the Tafel curve in a linear region (R^2>0.99) at an overpotential of 0.06 V to 0.08 V was shown in Fig 6(b). The intersection of the fitted line and the y-axis was the logarithm of the exchange current densities (i_0). The corresponding linear equations and exchange current density values are listed in the table 4. The PMo/CB were dramatically higher than that of CB

(0.055 mA/cm^2). In addition, the exchange current density of PMo/CB-2 (0.449 mA/cm^2) was higher than that of Pt/C (0.398 mA/cm^2) and even higher than the exchange current density value of CoPP-POM/C catalyst (2.28×10^{-9} mA/cm^2) [53]. This showed that PMo/CB exhibited effective electron conversion ability and high electronic utilization efficiency for ORR. The electronic conversion capability and utilization efficiency of PMo/CB gradually decrease from PMo/CB-2 to PMo/CB-4. This is also mutually confirmed with the LSV results. In general, the results indicate that PMo play an important role for the efficient ORR, and the best electrocatalytic activity is obtained from PMo/CB-2 with the optimal component. PMo/CB-2 has excellent ORR activity and low cost and a highly prospect as a Pt-substituted ORR catalyst for microbial electrochemical systems.

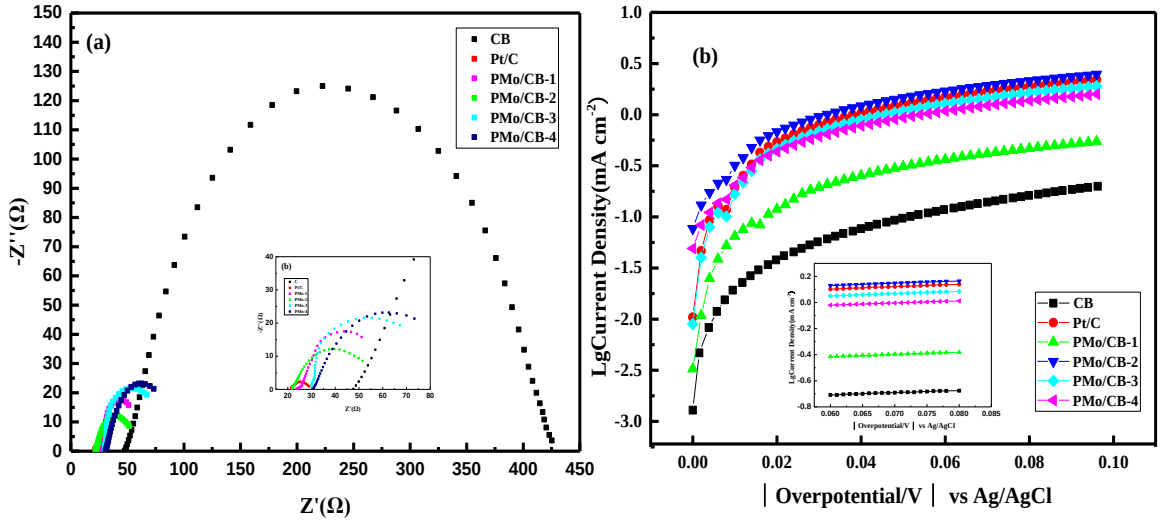

Figure 6. (a) Nyquist plots of electrochemical impedance spectroscopy for different catalysts measured by EIS device. (b) The linear fit for the Tafel plots of PMo/CB at the overpotential from 60 to 80 mV.

Table 3. The results of equivalent circuit fitting of samples

Resistance	CB	Pt/C	PMo/CB-1	PMo/CB-2	PMo/CB-3	PMo/CB-4
R_{act}(Ω)	47.7	21.4	23.9	21.8	30	30.6
R_{ohm}(Ω)	377.3	8.6	43.6	33.2	35	49.4

Table 4. The calculating exchange current density by linear fitting of Tafel curves

Sample	Linear fitting equation	R^2	i_0(mA/cm^2)
CB	y=0.9132x - 1.257	0.9990	0.0552
Pt/C	y= 0.8453x - 0.399	0.9980	0.398
PMo/CB-1	y= 0.7509x - 0.860	0.9985	0.138
PMo/CB-2	y= 0.8036x - 0.348	0.9982	0.449
PMo/CB-3	y= 0.7334x - 0.383	0.9952	0.414
PMo/CB-4	y= 0.7424x - 0.462	0.9985	0.345

3.3.MFC performance of PMo/CB catalysts

The performance of the PMo/CB in the microbial electrochemical system was investigated, and MFC was started to observe its power generation. Different external resistors were adjusted to obtain a polarization curve, an anode potential curve and a power density curve after the MFC was stable for one month. The power density curves were shown in Fig 7(a). Remarkably, the power density of PMo/CB-2-MFC (1195.1 ± 41.7 mW/m^2) was 5.44 times higher than the control (with CB) (219.6 ± 11.0 mW/m^2). The maximum power density of PMo/CB-2-MFC compared those of PMo/CB-3-MFC (900.4 ± 24.9 mW/m^2) and PMo/CB-4-MFC (718.3 ± 39.4 mW/m^2) increased by 32.7% and 66.4% respectively. The PMo/CB-1-MFC had a poor behaviour (606.4 ± 24.8 mW/m^2), this also implied a poor ORR activity of PMo/CB-1in the MFC. Additionally, maximum power densities of PMo/CB-2-MFC were also higher than that of Pt/C-MFC (984.2 ± 62.2 mW/m^2), which were increased by 21.4%. It was suggested that PMo/CB-2 had a better promoting effect on the performance of MFC. The power density of the PMo/CB-2-MFC was similar or even higher than that of the MFC previously reported (table 5) [6, 54-58]. The electrode potential curve of MFC showed in Fig 7(b). It can be seen that the anode potential of all MFCs was almost the same, and cathodic potential response was different. This fully proved that the enhanced power generation of MFC was mainly due to the higher ORR activity on the air-cathode. Thus, these results further confirmed that the hybrid of CB with appropriate PMo (10 wt%) substantially enhanced its ORR kinetics and could be responsible for higher power output of MFC.

The power output of the MFC during long-term operation was showed in the fig 7(c). It can be seen that The Pt/C-MFC had greatly reduced power production, with a 76% reduction in maximum power to 300 ± 10 mW/m^2, and the PMo-MFC was only reduced by 16.9% after a continuous operation for 3 months. After 4 months of operation, PMo/C-2-MFC always maintains a high power density (900 ± 21 mW/m^2), but the power density of Pt/C-MFC was only 280 ± 56 mW/m^2. This result indicated that PMo/C-2 kept long-term stable ORR activity as electrocatalyst of the air-cathode in MFC.

Hence, in order to verify and clarify the above experimental results in real MFC, further measurements including chronoamperometry and LSV experiments were carried out on real MFC with the PMo/CB and Pt/C. Chronoamperometry tests showed that the performance was enhanced with PMo/CB-2-MFC (Figure 7(d)). The open circuit potential (OCP) of PMo/CB-2-MFC was slightly higher than that of Pt/C-MFC (0.248 V). The PMo/CB-2-MFC generated the highest current density of 5.84 A/m^2 at -0.2 V, which was 48.6% higher than Pt/C-MFC (3.93 A/m^2) at a potential of -0.2 V. Moreover, LSV plots of MFCs were depicted in Fig 7(e). The limit current density of PMo/CB-2-MFC was obviously higher than that of Pt/C-MFC from 0.4 V to -0.6 V, indicating hybrid of CB with PMo had the actual distinct activity of ORR in real MFCs. At the potential of -0.1V, PMo/CB-2-MFC reached the maximum limit current density (8.32 A/m^2), which was 1.1 times higher than that of Pt/C-MFC. Those are exactly consistent with the maximum power density produced by MFC. The above results can greatly address and explain why PMo/CB-2-MFC exhibited the interesting power density.

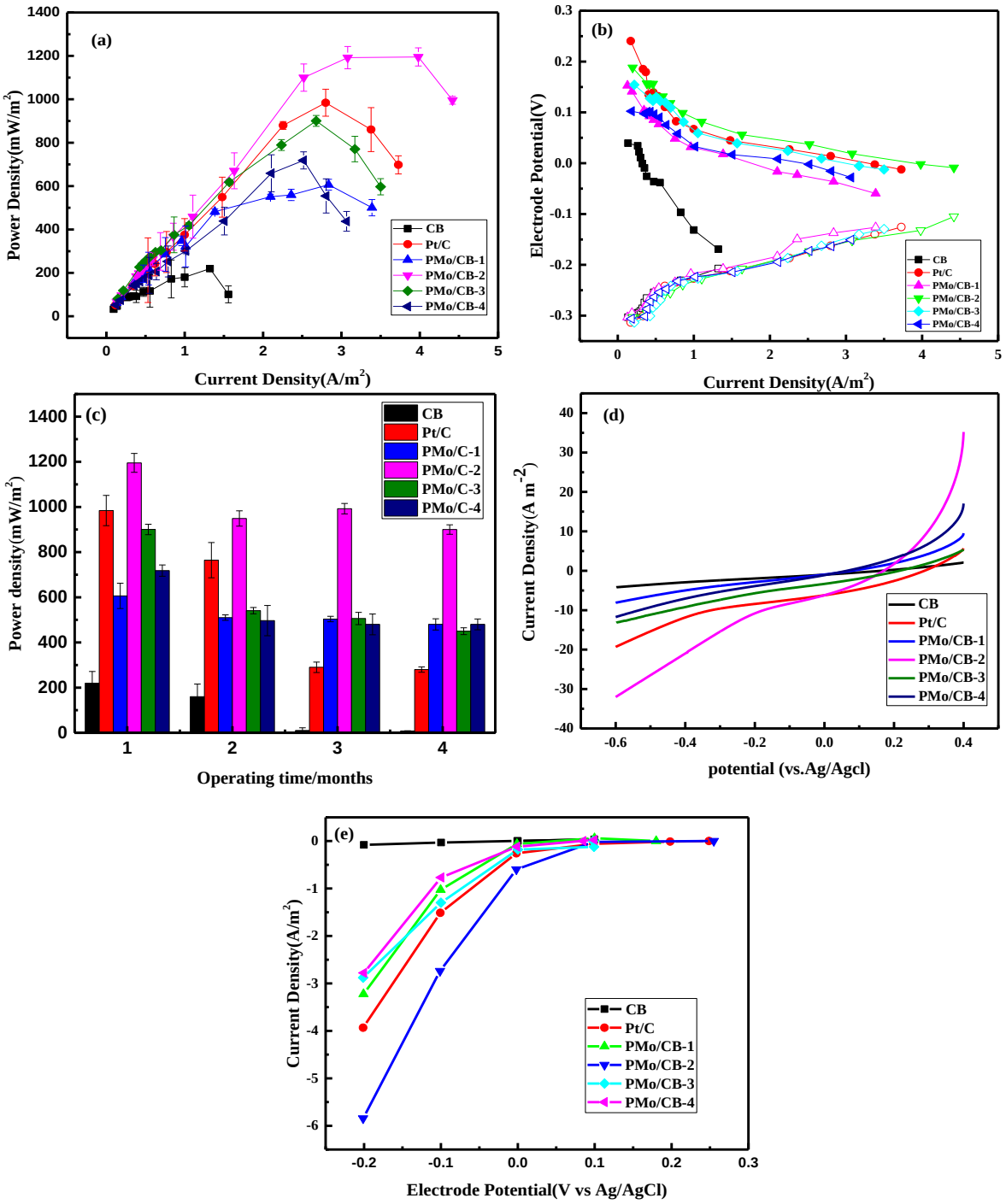

Figure 7. (a) The power density curves of MFCs with different samples (b) Electrode potentials of PMo/CB-MFC. Hollow dots represent cathode potential. (c) Power density output of different air-cathode MFCs during four months. (d) Current- potential curve of MFCs with different air-cathodes. (e) LSV plots of Pt/C-MFC and PMo/CB-MFCs. Both chrono-current and LSV curves are air-cathode, bio-anode and Ag/AgCl as working electrode, counter electrode and reference electrode respectively.

Table 5. Comparison of catalytic performance of carbon mixed ORR catalysts in MFC

Authors	Reported ORR catalyst	Number of transferred electrons	MFC power density output	high stability	Reference
Zhang et al	Activated Carbon /Carbon Black	2.9	1560 ± 40 mW/m^2	Yes	[6]
Ahmed et al	C–CoO_x–FePc	-	654 ± 32 mW/m^2	Yes	[54]
Zhang et al	MnO_2/CNTs	-	210 mW/m^2	Yes	[55]
Fu et al	NSFe_3O_4/AC	3.9	1430 mW/m^2	Yes	[56]
Birry et al	FePc/C	-	820 mW/m^2	Yes	[57]
Liu et al	LCCF/C	-	405 mW/m^2	Yes	[58]
This work	$H_3PMo_{12}O_{40}$/CB	3.9	1195.1 ± 41.7 mW/m^2	Yes	

3.4 Mechanism Analysis

According to the above analysis, the possible ORR mechanism of PMo/CB was speculated and depicted in Fig 8. The CB has more conductive channels and oxygen molecule attachment points due to its excellent electrical conductivity and high specific surface area [59].

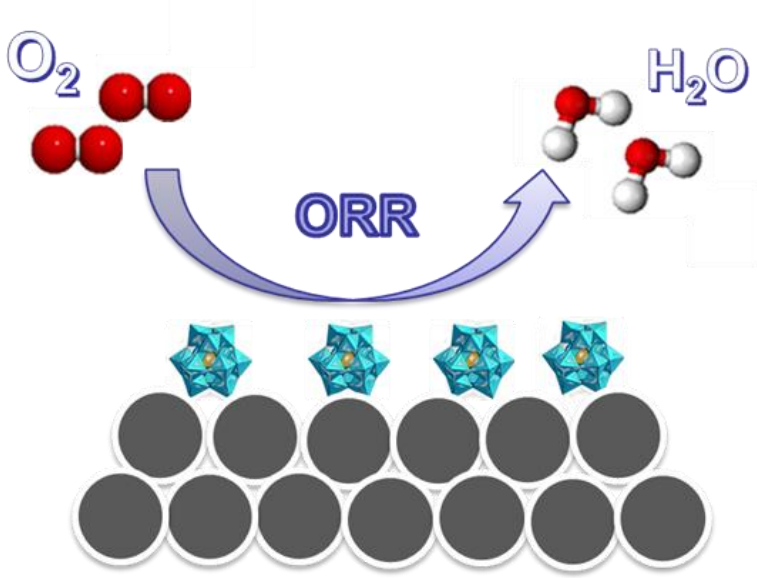

Figure 8. The principle illustration of the oxygen reduction process on the PMo/CB surface

After PMo is loaded on CB, the multivalent Mo ion (Mo^{4+}, Mo^{6+}) in active PMo structure enhances the ORR electron transfer rate, and the special Keggin structure further improves the rate of absorption of oxygen atoms [60, 61]. The electronic coupling between PMo and CB promotes the more

electrons transfer from PMo to CB. This interaction may cause a significant decrease in the local electron density near the PMo site, which may enhance the chemisorption of O_2 [62, 63]. In addition, the hydrophilicity of PMo/CB is also beneficial to the adsorption and reduction of O_2. However, as the PMo component increases, the catalytic activity of the sample decreases. This can be attributed to its smaller BET surface area, which blocked the adhesion of oxygen molecular to the PMo/CB surface. Thus, adjusting the proportions of PMo could be more favorable for ORR. Overall, it could be surmised that the synergistic integration of CB and PMo in the prepared sample gave rise to the excellent ORR activity.

4. CONCLUSIONS

In this work, PMo/CB was prepared and used as a catalyst to facilitate ORR in the air-cathode of MFCs. PMo/CB-2 exhibited distinct ORR activity in electrolyte. The results of Koutecky-Levich plot revealed that the ORR process occurs with the mechanism of the four-electron for PMo/CB-2. The PMo/CB-2-MFC achieved a maximum power density of 1195.1±41.7mW/m^2. The power density of PMo/CB-2-MFC is always higher than that of Pt/C even if all MFC production was reduced during the four months of MFC operation. Thence, PMo/CB can be an important alternative to platinum for the application of microbial electrochemical system in environmental monitoring and strengthening the degradation of pollutants.

ACKNOWLEDGMENTS
This work was financially supported by the Natural Science Foundation of China (51778083), the Scientific Research Foundation (2011DA105287-ZD201801) of State Key Laboratory of Coal Mine Disaster Dynamics and Control, the Natural Science Foundation of Chongqing in China (cstc2017jcyjBX0042) and the Chongqing Research Program of Basic Research and Frontier Technology (cstc2016jcyjA0506).

References

1. B.E. Logan, *Nat Rev Microbiol*, 7 (2009) 375.
2. K. Rabaey and W. Verstraete, *Trends Biotechnol*, 23 (2005) 291.
3. Y.Y. Liu, L.Y. Shen, P.F. Song, D.M. Chang, Z.H. Lu and Y.D. Liu, *Int. J. Electrochem. Sci*., 14 (2019) 196.
4. H. Rismaniyazdi, SM. Carver, A.D. Christy and O. H. Tuovinen, *J. Power Sources*,180 (2008) 683.
5. S. Cheng and B.E. Logan, *Bioresource Technol*, 102 (2011) 4468.
6. X. Zhang, X. Xia, I. Ivanov, X. Huang and B. E. Logan, *Environ Sci Technol*, 48 (2014) 2075.
7. W. He, W. Wu and Z.H. Tang, *Int. J. Electrochem. Sci*., 13 (2018) 4438.
8. X. Xia, F. Zhang, X. Zhang, P. Liang, X. Huang and B.E. Logan, *ACS Appl Mater Inter*, 5 (2013) 7862.
9. X. Zhang, S. Cheng, X. Wang, X. Huang and B.E. Logan, *Environ Sci Technol*, 43 (2009) 8456.
10. Z. Liu, F. Peng, H. Wang, H. Yu and W. Zheng, *Angew Chem Int Edit*, 50 (2011) 3257.
11. L. Yang, S. Jiang, Y. Zhao, L. Zhu, S. Chen and X. Wang, *Angew Chem Int Edit*, 50 (2011) 7132.
12. T. Yang, K. Li, L. Pu, Z. Liu, B. Ge, Y. Pan and Y.Liu, *Biosens Bioelectron*, 129 (2016) 233.
13. L. Qu, Y. Liu, J. Baek and L. Dai, *ACS Nano*, 4 (2010) 1321.

14. Z. Chen, D. Higgins and Z. Chen, *Carbon*, 48 (2010) 3057.
15. D. Kim, O.L. Li and N. Saito, *Phys Chem Chem Phys*, 17 (2015) 407.
16. L. Yao, W.H. Zhong, L. Qiu and L. Deng, *Int. J. Electrochem. Sci*., 13 (2018) 5798.
17. L. Li, X. Yuan and Z. Ma, J. *Electrochem. Soc*, 162 (2015) F359.
18. L.S. Madis, H.K. Erikson and M.D. Merisalu, *J. Electroanal Chem.*, 834 (2019) 223.
19. M.J. Choi, E.T. Yang and H.W. Yu, *Int. J. Hydrogen Energ*, 44 (2019) 2258.
20. C.Z. Zhu and S.J. Dong, *Nanoscale*, 5 (2013) 1753.
21. J.S. Lee, L. Cheolmin and Y.L. Jae, *ACS Catal*, 8 (2018) 7213.
22. C.L. Hill, *Coordin Chem Rev*, 143 (1995) 407.
23. Y. Song and R. Tsunashima, *Chem Soc Rev*, 41 (2012) 7384.
24. D.L. Long, R. Tsunashima and L. Cronin, *Chem., Int. Ed*, 49 (2010) 1736.
25. H.N. Miras, J. Yan, D.L. Long and L. Cronin, *Chem. Soc. Rev*, 41 (2012) 7403.
26. H.J. Lv, Y.V. Geletii, C.C. Zhao, J.W. Vickers, G.B. Zhu, Z. Luo, J. Song and T.Q. Lian, *Chem. Soc. Rev*, 41 (2012) 7572.
27. A. Proust, B. Matt, R. Villanneau, G. Guillemot, P. Gouzerh and G. Izzet, *Chem. Soc. Rev*, 41 (2012) 7605.
28. C. Freire, D.M. Fernandes, M. Nunes and V.K. Abdelkader, *Chemcatchem,* 10 (2018) 1703.
29. M. Sadakane and E. Steckhan, *Chem. Rev.*, 98 (1998) 219.
30. D.M. Fernandes and C. Freire, *ChemElectroChem*, 2 (2015) 269.
31. N. Marta, M. Diana, I. M. Fernandes and F.R. Manuel, *ChemistrySelect*, 1 (2016) 6257.
32. X.H Xie, Y. Nie, S. Chen, W. Ding, X.Q. Qi and L. Li, *J. Mater. Chem. A*, 3 (2015) 13962.
33. M. F. Diana, C.N. Hugo and B. Revathi, *Langmuir*, 34 (2018) 6376.
34. E. Antolini, *Appl Catal B Environ*, 88 (2009) 1.
35. L. Feng, Y. Yan, Y. Chen and L. Wang, *Energ Environ Sci*, 4 (2011) 1892.
36. B.E. Logan, B. Hamelers, R. Rozendal, U. Schrorder, J. Keller, S. Freguia, P. Aelterman, W. Verstraete, K. Rabaey, P. Aelterman, W. Verstraete and K. Rabaey, *Environ. Sci. Technol*, 40 (2006) 5181.
37. B. Zhang, H. Asakura and J. Zhang, *Angew Chem Int Edit*, 55 (2016) 8319.
38. N. Zhu, Y. Lu and B. Liu, *J. Nanopart Res*, 19 (2017) 457.
39. A. Popa, V. Sasca and D. Bajukbogdanovic, *J. Therm Anal Calorim*, 126 (2016) 1567.
40. T. Ma, Y. Cao and H. Chen, *Colloid Surface A*, 43 (2018)212.
41. H.P. Boehm, *Carbon*, 32 (1994) 759.
42. M. Sujata, R. Surjyakanta, and P. Kulamani, *Ind Eng Chem Res*, 51 (2012) 7859.
43. V. Balaga, J. Pedada, H.B. Friedrich and S. Singh, *J. Mol Catal A*, 425 (2016) 116.
44. Z. Bowen, X.Y. Yue, H. Li and J.F. Li, *Reac Kinet Mech Cat*, 125 (2018) 55.
45. G. Gnana, Z. A. Kumar, K.S. Nahm and J.S. Xavier, *Biosens Bioelectron*, 53 (2014) 528.
46. Y. Su, Y. Zhu, X. Yang, J. Shen, J. Lu, X. Zhang, J. Chen and C. Li, *Ind. Eng. Chem. Res*, 52 (2013) 6076.
47. L. Zhang, Y. Hu and J. Chen, *J. Power Sources*, 98 (2018) 213.
48. U. A. Paulus, A. Wokaun, G. G. Scherer, T. J. Schmidt, V. Stamenkovic, V. Radmilovic, N. M. Markovic, P. N. Ross, *J. Phys.Chem. B*, 106 (2002) 4181.
49. X. Yu, W. Yin, T. Wang, *Langmuir*, 35 (2019) 2909.
50. R. Kumar, L. Singh and A.W. Zularisam, *Int. J. Hydrogen Energ*, 42 (2017) 19287.
51. M. Sun, F. Zhang, Z. Tong, G. Sheng, Y. Chen, Y. Zhao and H. Yu, *Biosens Bioelectron*, 26 (2010) 338.
52. R. Kumar, L. Singh, A.W. Zularisam and F.I. Hai, *Bioresource Technol*, 537 (2016) 21.
53. M. Nagai, H. Sanpei, M. Shirakura, *J. Mater. Chem.*, 22 (2012) 9222.
54. J. Ahmed, Y. Yuan and L. Zhou, *J. Power Sources*, 208 (2012) 170.
55. Y. Zhang, Y. Hu and S. Li, *J. Power Sources*, 196 (2011) 9284.
56. Z. Fu, L.T. Yan and K.X. Li, *Biosens Bioelectron*, 74 (2015) 989.

57. L. Birry, P. Mehta and F. Jaouen, *Electrochim Acta*, 56 (2011) 1505
58. H. Dong, H.B. Yu and X. Wang, *J. Chem Technol Biotechnol*, 88 (2013) 774.
59. M. Nasibi, M.A. Golozar and G. Rashed, *Mater Chem Phys*, 139 (2013) 12.
60. Y. Liu, J. He, W. Chu and W. Yang, *Catal Sci Technol*, 8 (2018) 5774.
61. L.B. Yang, X. F. Wang, A.J. Xie, G. Hu and Y.H. Shen, *Front. Mater. Sci. China*, 3 (2009) 1.
62. X. Yu, R. Du, B. Li, L. Liu and Y. Zhang, *J. Phys. Chem. C*, 121 (2017) 6712.
63. J. Yang and J. Ying, *Angew. Chem., Int. Ed*, 50 (2011) 4637.